Title

Identifying the Role of Dynamic Surface Hydroxides in the Dehydrogenation of Ti-Doped NaAlH4

Journal

ACS Applied Materials & Interfaces, 11(5)

ISSN

1944-8244

Authors

White, James L
Rowberg, Andrew JE
Wan, Liwen F
et al.

Publication Date

2019-02-06

DOI

10.1021/acsami.8b17650

Peer reviewed

Identifying the Role of Dynamic Surface Hydroxides in the Dehydrogenation of Ti-Doped $NaAlH_4$

James L. White,[†] Andrew J. E. Rowberg,[‡,§] Liwen F. Wan,[‡,∥] ShinYoung Kang,[‡] Tadashi Ogitsu,[‡] Robert D. Kolasinski,[†] Josh A. Whaley,[†] Alexander A. Baker,[‡] Jonathan R. I. Lee,[‡] Yi-Sheng Liu,[∥] Lena Trotochaud,[∥] Jinghua Guo,[∥] Vitalie Stavila,[†] David Prendergast,[∥] Hendrik Bluhm,[∥] Mark D. Allendorf,[†] Brandon C. Wood,*[,‡] and Farid El Gabaly*[,†]

[†]Sandia National Laboratories, Livermore, California 94550, United States

[‡]Lawrence Livermore National Laboratory, Livermore, California 94550, United States

[§]University of California Santa Barbara, Santa Barbara, California 93106, United States

[∥]Lawrence Berkeley National Laboratory, Berkeley, California 94720, United States

ABSTRACT: Solid-state metal hydrides are prime candidates to replace compressed hydrogen for fuel cell vehicles due to their high volumetric capacities. Sodium aluminum hydride has long been studied as an archetype for higher-capacity metal hydrides, with improved reversibility demonstrated through the addition of titanium catalysts; however, atomistic mechanisms for surface processes, including hydrogen desorption, are still uncertain. Here, operando and ex situ measurements from a suite of diagnostic tools probing multiple length scales are combined with ab initio simulations to provide a detailed and unbiased view of the evolution of the surface chemistry during hydrogen release. In contrast to some previously proposed mechanisms, the titanium dopant does not directly facilitate desorption at the surface. Instead, oxidized surface species, even on well-protected $NaAlH_4$ samples, evolve during dehydrogenation to form surface hydroxides with differing levels of hydrogen saturation. Additionally, the presence of these oxidized species leads to considerably lower computed barriers for H_2 formation compared to pristine hydride surfaces, suggesting that oxygen may actively participate in hydrogen release, rather than merely inhibiting diffusion as is commonly presumed. These results demonstrate how close experiment–theory feedback can elucidate mechanistic understanding of complex metal hydride chemistry and potentially impactful roles of unavoidable surface impurities.

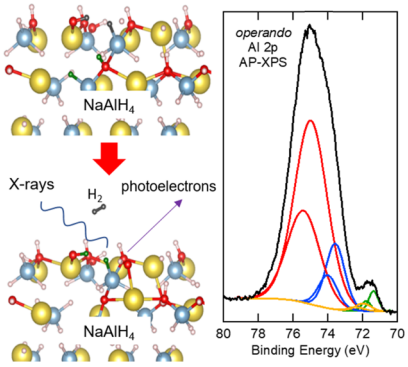

INTRODUCTION

Hydrogen-powered fuel cell vehicles are now a commercial reality, with a small number of automobiles being sold by original equipment manufacturers. Clean hydrogen-based energy technologies, such as vehicular fuel cells, typically require efficient storage of hydrogen. Current commercial hydrogen storage approaches employ high-pressure (35–70 MPa) gas or cryogenic (20 K) liquid hydrogen. However, these systems have limited volumetric energy densities, especially when the tanks and other components essential to maintaining the pressures or temperatures are considered. Solid metal hydrides, particularly complex metal hydrides, are of interest due to their high volumetric H content (>150 kg H_2 m^{-3}) compared to compressed gas (~24 kg H_2 m^{-3} system) or cryogenic liquid storage (~70 kg H_2 m^{-3}, not including the system). Only solid hydride systems are capable of meeting the ultimate U.S. Department of Energy (DOE) volumetric energy density target (50 kg H_2 m^{-3} system).[1]

The primary issues surrounding complex metal hydrides are their sluggish kinetics and poor reversibility since many high-capacity materials have high decomposition barriers or undesired side reactions that lead to kinetically stable products that no longer participate in the (de)hydrogenation processes.[2] One method to improve cyclability is the addition of non-noble transition metals or rare-earth elements to catalyze the reactions. Titanium-containing species are the most widely used and can enable reversibility at much lower temperatures and pressures than the pure hydride, even at concentrations as low as 0.5 mol %.[3−8] This empirical doping technique, pioneered by Bogdanović and co-workers in 1997 on the complex metal hydride archetype sodium aluminum hydride ($NaAlH_4$),[9] was found to lower the dehydrogenation onset

temperature compared with undoped $NaAlH_4$ (150 vs 265 °C) to enable reversibility.

Although $NaAlH_4$, which can reversibly store only 5.5 wt % hydrogen, lacks sufficient capacity to meet DOE targets, this catalyzed system nevertheless remains a model system for understanding and improving more promising complex metal hydrides, such as $Mg(BH_4)_2$ (14.9 wt %). In the intervening twenty years since Bogdanović's pioneering work, many studies, both experimental and theoretical, have been published concerning the detailed mechanism of dehydrogenation and the role of titanium in Ti-doped $NaAlH_4$ in improving the kinetics of the reactions (eqs 1 and 2).

$$3NaAlH_4 \rightarrow Na_3AlH_6 + 2Al + 3H_2 \quad (1)$$

$$Na_3AlH_6 \rightarrow 3NaH + Al + \frac{3}{2}H_2 \quad (2)$$

Multiple interpretations have been posited describing possibly relevant Ti-containing surface and bulk phases that are generated in the cycling process.[10,11] Proposed mechanisms for H_2 evolution catalysis include Ti substitution into the lattice (on Na, Al, or both cation sites),[12,13] formation of Ti–Al alloys,[7,14−17] and localization of metallic Ti on the surface.[5,18,19] However, experiments performed under a wide range of conditions lead to conflicting conclusions, which have been detailed and critiqued in depth in the review by Frankcombe.[10] Consequently, the precise mechanism by which this archetypical catalyst enables reversible H_2 release remains unresolved.

The mechanistic controversy over the role of Ti in $NaAlH_4$ underscores a deeper knowledge gap concerning the surface processes that govern the exchange of hydrogen gas with solid complex metal hydrides. A better understanding of these processes would be extremely valuable for devising strategies to improve the kinetics further, not just for $NaAlH_4$ but also for other, more promising hydrides, both doped and undoped. Unfortunately, the limited number of reports concerning the surface chemistry of hydrides emphasizes how challenging it is to characterize the operando, out-of-equilibrium gas–solid interface with chemically sensitive spectroscopies and microscopies. The hydrogenation process is particularly difficult as it often occurs at substantial overpressures, effectively limiting operando chemical characterization to dehydrogenation, where elevated pressures can be avoided.

As a general rule, investigations of surface processes have often neglected the potential role of surface contaminants present beyond those introduced intentionally as a result of titanium or other doping. This omission is to the detriment of a holistic understanding of the system and tends to bias interpretations of the surface chemistry. Indeed, oxygen contamination is an omnipresent concern with these highly reactive metal hydrides. It is very difficult to shield a hydride completely ($\ll$0.01 ppm O_2 or H_2O) from oxidants throughout the entirety of its synthesis, processing, and cycling, leading to the presence of oxidized species at the surface, even though the bulk of the material may be maintained in apparently pristine condition. Recrystallization of $NaAlH_4$ from tetrahydrofuran has usually been employed experimentally to remove bulk impurities,[20−22] as shown by a variety of techniques, such as X-ray absorption spectroscopy (XAS),[20,23,24] X-ray diffraction (XRD),[15,17,25] and NMR.[26,27] However, the composition of the first few nanometers of the surface can differ substantially from the interior due to interactions with trace oxygen in gloveboxes and Schlenk lines, regardless of cleanliness. Describing the role of these incidentally oxygenated surfaces operando (during dehydrogenation) and offering an unbiased interpretation of the accompanying surface chemistry are essential to gain a complete perspective of potential kinetic limitations in the overall material.

The possible roles of surface oxide in hydrogen release mechanisms are numerous. A fully oxidized surface could be an inert observer, or it may present a passivating or blocking layer that prevents hydrogen flux in addition to detracting from the overall storage capacity.[28] However, fast hydrogen transport on some oxide surfaces has been demonstrated over short distances, suggesting that this behavior is not universal.[29] Surface oxides could also play a more direct role in the surface reactions themselves. This possibility was suggested by Delmelle et al.,[30] who studied the role of oxide surface contamination in the dehydrogenation of Ti-doped $NaAlH_4$ using in situ X-ray photoelectron spectroscopy (XPS). Based on the evolution of Ti, Al, and O XPS spectra, and using reference XPS binding energies to identify features corresponding to $NaAlH_4$, Al_2O_3, and metallic Al, they suggested that oxygen shuttles reversibly between titanium and aluminum oxides. Within their interpretation, the enhanced dehydrogenation kinetics of Ti-doped $NaAlH_4$ are due to the higher hydrogen mobility in titanium oxides than aluminum oxides.

To address these issues and gain a much more complete understanding of the role of surface oxides and titanium on $NaAlH_4$ desorption, we employed a comprehensive suite of operando and ex situ characterization methods, together with ab initio surface simulations to probe the evolution of surface and subsurface chemical species of previously cycled $TiCl_3$-doped $NaAlH_4$. On the experimental side, we combined three operando surface science techniques—ambient-pressure X-ray photoelectron spectroscopy (AP-XPS) and Auger electron spectroscopy (AES) for the surface and immediate subsurface (2–3 nm) and low-energy ion scattering (LEIS) for the topmost monolayer—with ex situ scanning transmission X-ray microscopy (STXM) of the bulk. On the theory side, we employ ab initio molecular dynamics (AIMD) and direct XPS simulations based on density functional theory (DFT) calculations to provide unbiased guidance for experimental interpretation in this changing system. This integrated experiment/theory approach allowed us to probe all relevant length scales influencing the surface mechanism of H_2 release, resulting in a more complete interpretation of the evolution and possible role of surface oxide in $NaAlH_4$.

We find that residual amounts of oxide at the surface of Ti-doped $NaAlH_4$ evolve continuously during dehydrogenation, transitioning among different degrees of protonation as the subsurface reaction initiates. This suggests that the oxide may play a critical role in facilitating H_2 formation through a hydroxide-mediated reaction, controlling the surface rate for H_2 evolution and likely also the overall dehydrogenation rate. We also find that, although titanium unquestionably improves the kinetics of H_2 release from $NaAlH_4$, this element was not detected by either AP-XPS or LEIS, demonstrating that it plays no direct role in promoting surface reactions.

RESULTS AND DISCUSSION

Surface Composition Analysis. *X-ray Photoelectron Spectroscopy.* A complete thermally driven dehydrogenation of previously cycled 10 mol % $TiCl_3$-doped $NaAlH_4$ was

performed using synchrotron-based AP-XPS to monitor all surface and subsurface (~3 nm) chemical species operando. The $NaAlH_4$ used was previously cycled, rather than freshly ball milled, in order to emulate more closely a realistic system akin to one that would be present in a fuel cell vehicle after a number of uses and to reach more of a steady state in its behavior. The sample was protected from exposure to air and moisture from the recrystallization to characterization in an argon glovebox (P_{O_2}, P_{H_2O} < 0.1 ppm) and using custom-made ultrahigh vacuum-grade clean transfer cases. Concurrent with the AP-XPS experiment, the gas within a few millimeters of the complex metal hydride surface was sampled with a differentially pumped cone, which led to a mass spectrometer. The hydrogen desorption was thus monitored continuously as the material was heated (Figure S1). Once heating began, the initial H_2 release was slow but increased drastically as the set temperature was elevated above 150 °C and even more so at 200 °C. The amounts of other gases detected, including H_2O, O_2, and N_2, did not vary significantly over the course of the experiment.

The atomic composition at the surface of the 10 mol % $TiCl_3$-doped $NaAlH_4$ was determined from the XPS broad survey spectra taken occasionally throughout the experiment at the two photon energies (PEs) of 735 and 440 eV (Figure S2) and calculated using the peak areas and the PE-dependent atomic cross sections from Yeh and Lindau.[31] As shown in Figure 1, the surface composition (43.7% Na, 6.6% Al, 0% Ti, 14.6% Cl, 6.5% C, and 28.6% O) differed drastically from the expected bulk composition of the material based on the doping level (41.7% Na, 41.7% Al, 4.2% Ti, and 12.5% Cl since H is not detectable by X-rays). At no point in the course of the in situ heating experiment was titanium observed in the survey spectra, at PEs of either 735 or 440 eV, even though an atomic concentration of 4.2% should be readily detectable. Even the detailed Ti 2p spectra, which should be able to detect concentrations as low as 0.1%, showed no peaks until near the end of the experiment after all the hydrogen had been desorbed, when very small peaks were observed (Figure S3). Similarly, a sample of the $TiCl_3$-doped $NaAlH_4$ that had been cycled and desorbed ex situ at 200 °C was also measured in indium foil, showing only small amounts of titanium (Figure S4). The titanium, although not present at the surface of the milled hydrogenated material before or during desorption, was observed within the first few nanometers of the solid–gas interface in the fully desorbed $NaAlH_4$. STXM showed that the titanium was in the metallic state, rather than the original Ti^{3+} state or a more oxidized Ti^{4+} state, throughout the bulk of both hydrogenated and dehydrogenated particles (Figure S5).

Over the course of the heating experiment, the evolution of the surface sodium environment expected from the chemical reactions was insufficient to cause substantial changes in the binding energy of the Na 1s (~1071 eV) or 2s (~64 eV) peaks. Likewise, the Cl 2p peaks (~198 eV), originally from the $TiCl_3$ dopant, had no significant shifts, indicating that they were unchanged during the course of desorption and likely were separate from the hydride and present only as inert NaCl, which was observed via XRD (Figure S6, Table S1).

Despite the samples being meticulously protected from exposure to air, large amounts of surface oxygen were found, as well as adventitious carbon, the latter of which was used at each time point as an internal reference to calibrate the peak energies.

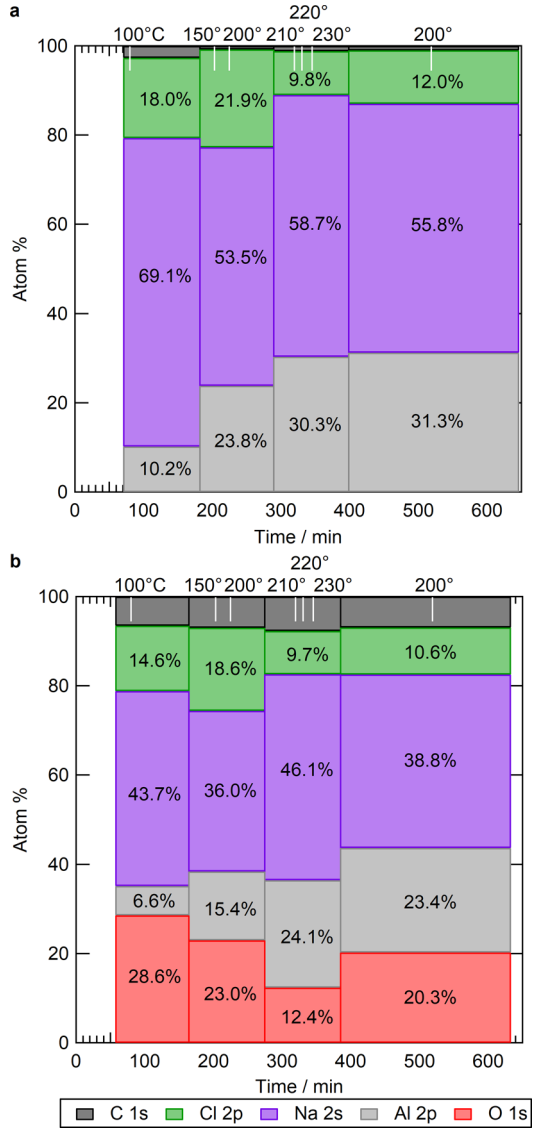

Figure 1. Atomic ratios obtained from XPS survey spectra at (a) PE = 440 eV and (b) PE = 735 eV over time, with the leftmost side of each bar indicating the ratios at that time. The indicated temperature values at various points signify the beginning of a new heating period. Note: O 1s (binding energy ~530 eV) is not detectable with PE = 440 eV.

Low-Energy Ion Scattering and Auger Electron Spectroscopy. Both LEIS and AES measurements independently corroborated the surface elements found by the AP-XPS experiment. AES revealed the presence of Na and Cl at the surface, as well as chemisorbed C and O impurities. This analysis did not reveal evidence of Ti. Similarly, comprehensive LEIS analysis over a wide range of experimental geometries did not reveal any evidence of Ti at the surface (Figure 2a). The primary motivation for using LEIS is that it is able to detect hydrogen at the surface, using direct recoil spectrometry on H atoms (Figure 2b), unlike all X-ray techniques, which can only infer the presence of hydrogen on the surface through changes in elements to which it is bound. Following the initial surface characterization, we heated the sample over a 45 min linear ramp from 25 °C up to 250 °C. During this time, we monitored the intensities of the scattering and recoil peaks associated with H, Na, Al, and the Pb substrate, the fourth due

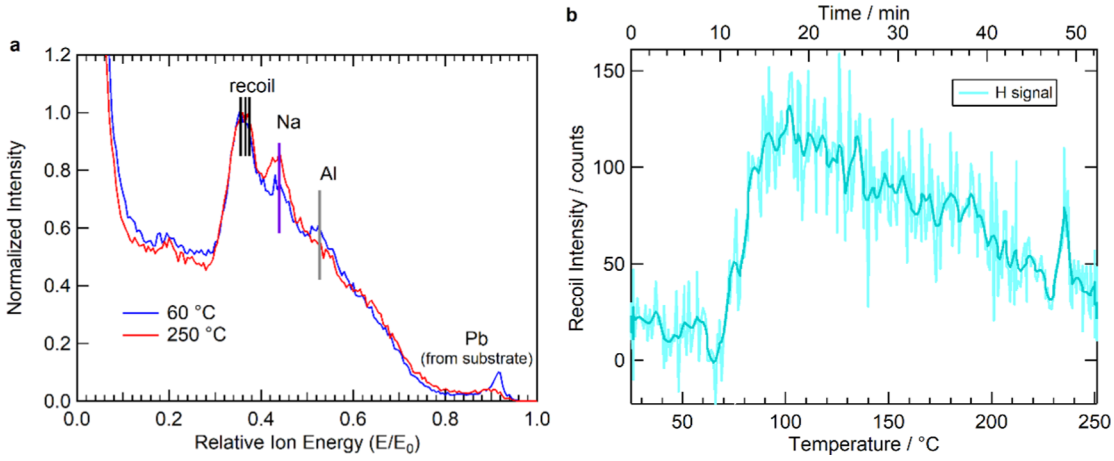

Figure 2. (a) Ion energy spectra of $TiCl_3$-doped $NaAlH_4$ at 60 °C (blue) and 250 °C (red). The horizontal scale is normalized to the incident beam energy (E_0). The theoretical locations of the Al, Na, and Pb scattering peaks, as well as several closely spaced recoil peaks, are indicated by the vertical lines. (b) Background-subtracted direct recoil spectrometry of hydrogen on the surface during desorption.

to gaps in the sample. Since the intensity of the recoiled H flux was small compared with the neighboring Na and Al signals, we monitored channels on either side of the H for background subtraction. Much of the noise in Figure 2b is due to this correction.

At temperatures above about 50 °C, H increasingly segregated to the surface and partially blocked the other elements from the ion beam. The signal slowly decreased toward the initial baseline as the hydrogen left the surface and desorbed as H_2 at higher temperatures. As with the AP-XPS measurements, sodium was initially found in slightly greater abundance than aluminum, and its signal further increased as the temperature rose, almost completely obscuring that of aluminum at 250 °C.

Identification of Surface Chemical Species. The Al 2p and O 1s regions of the AP-XPS spectra were found to be quite dynamic, suggesting that the surface chemistry associated with these elements is evolving during dehydrogenation. With the proper assignments of spectral features to surface motifs, our operando AP-XPS measurements allow for direct tracking of the evolution of chemical species at and near the surface during dehydrogenation.

Typical AP-XPS Al 2p and O 1s spectra at different points during the $NaAlH_4$ dehydrogenation reaction are shown in Figures 3 and 4, respectively. These highlight the difficulty of deconvoluting the spectral features, which can appear as distinct peaks or overlapping contributions. Unambiguous assignments are particularly challenging when multiple possible product species may be formed, especially given the spin−orbit coupling present in the Al 2p spectra. This is especially true for surface and near-surface chemistries that may not resemble bulk crystalline standards, such as those present and evolving in the operando AP-XPS experiment.

Aluminum. Past XPS studies on Al-containing compounds have reported ranges of Al 2p binding energies for Al metal (72.5−72.9 eV)[32−34] and Al_2O_3 (73.6−75.0 eV).[32,35−37] Different crystallographic arrangements of atoms on the surface and new species created by surface contamination also challenge the absolute peak assignment. For instance, the binding energy of AlOOH is reported as 73.9 eV in ref 48, whereas in ref 52 the intermediate surface Al−OH_x species is reported to have a peak at 74.4 eV, near the Al_2O_3 peak at 74.8 eV. Although the separation between metallic and oxidized aluminum is generally reported to be over 1 eV, the distinctions among the aluminum oxides and hydroxides are much smaller.

Al 2p peak assignments for $NaAlH_4$ and other aluminum hydrides have also varied. Values between 75.1 and 75.6 eV have been reported;[32,38] however, this range overlaps with oxide and hydroxide assignments and may in fact be improperly assigned due to partial surface oxidation. An interfacial Al−H species formed from the dissociation of water on clean Al was reported to have a peak at 72.4 eV, actually lower than the peak from the metal, rather than higher.[34,39] Moreover, to our knowledge, the peak positions of intermediate aluminum hydrides/hydroxides that can form during dehydrogenation of $NaAlH_4$, such as Na_3AlH_6, have not been reported.

To aid in the interpretation of Al 2p and O 1s spectra in this system undergoing potentially subtle chemical changes, we directly simulated XPS binding energies for reaction candidates using DFT.[40] We begin with a discussion of the computed Al 2p binding energies for candidate compounds (see the Experimental Section for details on the method). The calculated chemical shifts relative to Al^0 are shown as arrows in the top row of Figure 3a and tabulated in Table S2. In Figure 3a, we have aligned the computed and measured spectra by assuming that the lowest-binding-energy peak in the experiment corresponds to Na_3AlH_6, which is known to be present in the sample from the XRD pattern (see below). Note that the theory does not capture the doublet nature of the Al 2p peak since spin−orbit splitting was neglected.

The theoretical calculations show that the binding energy generally progresses in the order Al metal < Na_3AlH_6 < AlH_3 < $NaAlH_4$ < Al_2O_3 ≈ $Al(OH)_3$. This follows the logic that the more reduced Al species have lower XPS binding energies, whereas the more oxidized species have higher binding energies, with the hydride binding energies in between. This general interpretation is confirmed by Bader charge decomposition analysis,[41,42] which assigns a charge of +2.5 to Al in Al_2O_3 but only around +1.6 for $NaAlH_4$ and Na_3AlH_6. The relative ordering of $NaAlH_4$ and Na_3AlH_6 can also be explained since the Al−H bond is expected to be weaker in Na_3AlH_6.

At the same time, the calculations highlight the risk in making a priori assumptions regarding peak assignments in terms of the expected formal oxidation state. For instance, the

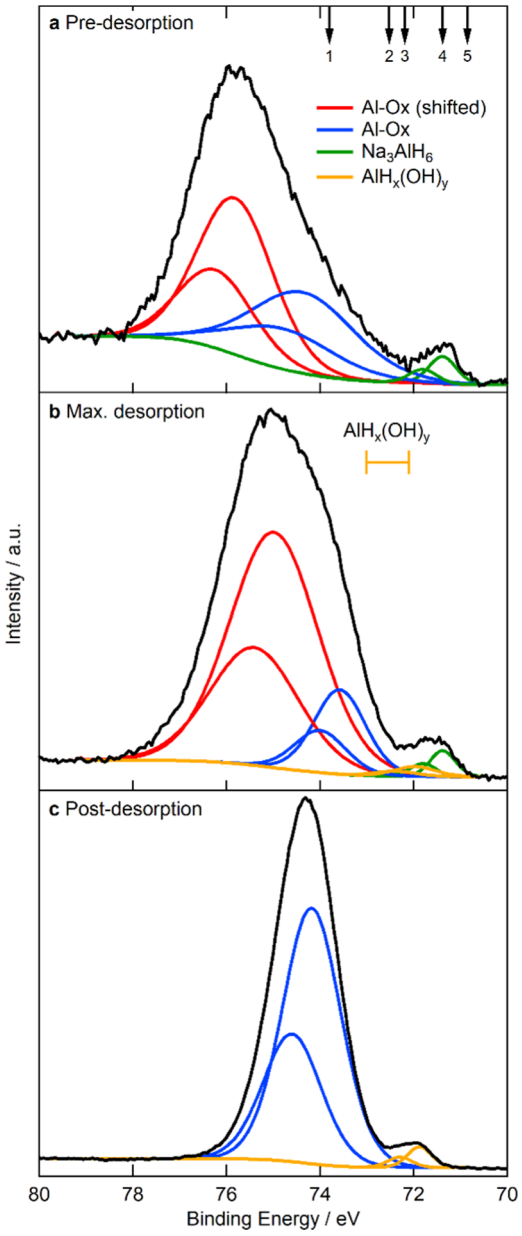

Figure 3. Al 2p AP-XPS spectra at PE = 440 eV (a) before desorption, (b) at maximum desorption, and (c) after desorption (while still at elevated temperature). Black lines are the raw data and colored lines are fitted contributions. The computed values for the bulk materials are shown as labeled black arrows at top (1) Al_2O_3/$Al(OH)_3$; (2) $NaAlH_4$; (3) AlH_3; (4) Na_3AlH_6; (5) Al metal. Computed binding energies for the AIMD-generated substoichiometric oxides fall within the orange range shown in (b).

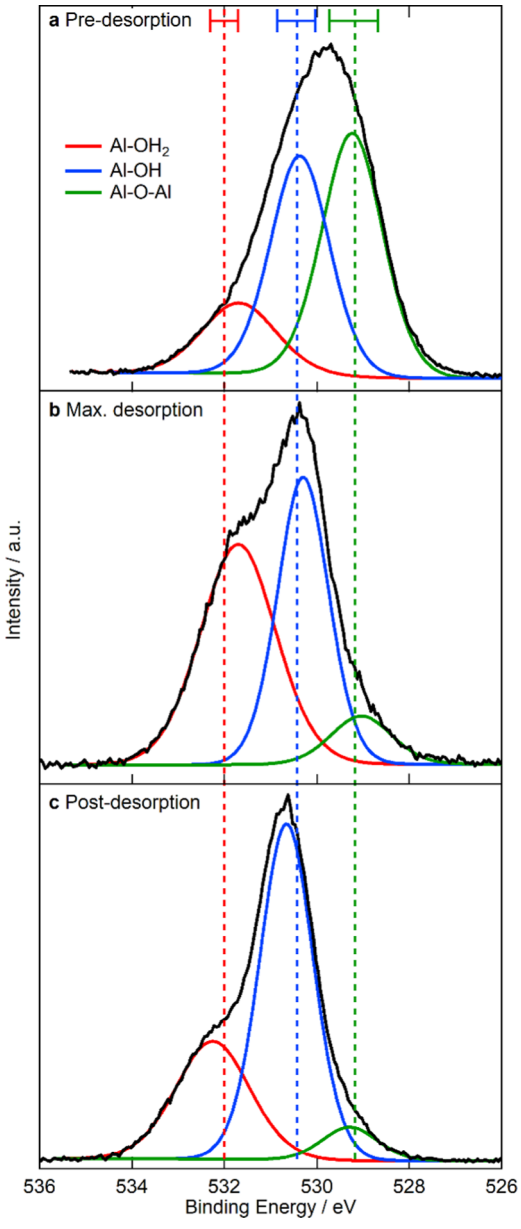

Figure 4. O 1s AP-XPS spectra (a) before desorption, (b) at maximum desorption, and (c) after desorption (while still at elevated temperature), adjusted for charging. Computed reference binding energies for the AIMD-derived substoichiometric oxide/hydroxide configurations are shown at top in (a). The dotted vertical lines and horizontal bars indicate the mean and extrema of the computed XPS binding energies from each of the three different types of oxygen coordination environments.

canonical interpretation of the two broad features around 71−72 and 73−76 eV in Figure 3 would assign the lower peaks to the Al^0 oxidation state (Al metal) and the higher peaks to Al^{3+} species (Al hydrides and oxides). This interpretation was assumed by Delmelle et al. and is widely reported in the literature.[30,38,43,44] However, Na_3AlH_6 conflicts with that interpretation since its computed binding energy is close to that of the Al metal. As a result, it should be difficult to distinguish between these two species within the lower-binding-energy feature.

Nevertheless, we can state with high confidence that the higher-binding-energy feature is likely dominated by the surface oxide and/or hydroxide, given both the abundance of oxygen detected by the survey spectra and the computed peak position. Additionally, we suggest that the lower-binding-energy region (<72 eV) is dominated by Al−H bonds. Although Al metal also falls within this range, it can be excluded from consideration because there should be little surface Al metal at the initial stages of dehydrogenation, and any exposed Al will quickly oxidize in the presence of the surface oxides and hydroxides. It is critical to note that the theoretical calculations conclude that at these lower binding energies, any Al−H signal must be derived from surface Na_3AlH_6-like species rather than the intuitively assumed

$NaAlH_4$. The formation of Na_3AlH_6 can be explained by considering the initial oxidation of AlH_4^- on the surface, which is likely to draw both hydrogen and aluminum from the sample, leaving behind a hydride species that is depleted with respect to these elements. In addition, the presence of Na_3AlH_6 in the cycled material may result from incomplete rehydrogenation, particularly at the surface. The formation of Na_3AlH_6 at the surface may also help explain the LEIS and XPS survey results, which show clear enrichment of Na relative to the amount expected for pure $NaAlH_4$, though some of that is likely also from NaCl formed from the reaction with $TiCl_3$. Within this interpretation, we can conclude that Na_3AlH_6-like species coexist with aluminum oxides and hydroxides in the outermost surface layer.

Based on the computational chemical shifts in conjunction with experimental literature values, the measured full Al 2p spectrum of recrystallized $NaAlH_4$ was first fitted by Al 2p doublets with features corresponding to oxidized Al (oxide/hydroxide) and Na_3AlH_6, separated by ~2.5 eV (Figure S7a). This same general assignment was then used in Figure 3 to study the evolving surface, as discussed in detail in the next section. Using Al K-edge total fluorescence yield X-ray absorption spectroscopy, which probes the samples more deeply than XPS, we confirmed that the oxide was limited to the surface of recrystallized $NaAlH_4$ by comparing it to a calculated spectrum of the pure material,[45] whereas the as-received $NaAlH_4$ had significant Al_2O_3 character (Figure S7b).

Oxygen. The composition of the surface oxide is highly dependent on the processing and exposure conditions as the hydride is milled, cycled, and transferred for analysis, regardless of the nominal cleanliness of the systems. Therefore, the changes, rather than initial conditions, of the oxide speciation over the course of the experiment are of interest in determining the surface behavior during hydrogen desorption. Although the bulk reference simulations are useful in broadly identifying the chemistry, the actual surface oxide will likely be substoichiometric and contain a richer variety of local bonding configurations. Accordingly, in addition to the bulk reference structures, we also generated oxidized surface configurations of both $NaAlH_4$ and Na_3AlH_6 from AIMD simulations. To do so, we followed the procedure of Pham et al. by incorporating oxygen into high-symmetry sites at the (001) surface in different concentrations and then relaxing the systems with DFT and running AIMD on the resulting systems to create realistic structures (see Figure S8 and Experimental Methods).[40]

The AIMD simulations of the oxidized Na−Al−H systems revealed O species with three distinct levels of proton/hydrogen coordination, corresponding to Al−O−Al, Al−OH, and $Al-OH_2$ motifs (the third resembled strongly bound, rather than weakly adsorbed, water). Of these three, the strongest preference was found for hydroxide formation, with AlH_x groups at various stages of conversion to $Al(OH)_x$ observed depending on the degree of O saturation. No Na−O bonds were detected. Several representative configurations were selected for computation of Al 2p and O 1s binding energies. The range of Al 2p binding energies for these $AlH_x(OH)_y$ configurations is shown at the top of Figure 3b. No distinct differences in the Al 2p energies were found among the Al−O−Al, Al−OH, and $Al-OH_2$ species. All three were found to lie at slightly lower binding energies than the bulk Al_2O_3 and $Al(OH)_3$ reference values, overlapping with $NaAlH_4$. This result highlights the difficulty in distinguishing among $NaAlH_4$, bulk oxides/hydroxides, and substoichiometric oxides/hydroxides, which fall in an almost continuous manifold.

Next, we discuss the computed O 1s XPS binding energies. Here, we again rely on configurations generated from AIMD of oxidized Na−Al−H since these are likely to be most representative of the actual surface oxide chemistry. Unlike the Al 2p binding energies, the O 1s values obtained from the AIMD simulations cluster neatly into three pools corresponding to the three distinct oxygen environments. The order of the binding energies follows the degree of hydrogen coordination according to Al−O−Al < Al−OH < $Al-OH_2$. Ranges of calculated binding energies for each of these three coordination environments are shown in Figure 4 and tabulated in Table S3. The experimental spectra in Figure 4 were fitted with three corresponding peaks, with the median simulated Al−O−Al peak aligned to the lowest-energy experimental fit. Because the O 1s spectrum produces fewer possibilities and more consistency between configurations in the AIMD simulation data, its interpretation is far less ambiguous.

Evolution of Surface Chemistry. Figures 3 and 4 show component fits to the experimental data, which are compared with the computed references to interpret how the surface chemistry of the cycled Ti-doped $NaAlH_4$ evolves during desorption. We point out that some differences are observed between the Al 2p AP-XPS signal in Figure 3 and the reference recrystallized $NaAlH_4$ sample in Figure S7. In particular, relative to the recrystallized sample, the hydride contribution in Figure 3 (green) on the surface is diminished and the contribution from oxide/hydroxide (red, blue) dominates the Al 2p AP-XPS signal. This difference in relative concentrations likely results from the additional handling of the material during ball milling and cycling, exposing it to a greater amount of potential contaminants over a longer period of time, as well as the lower photon energy (440 vs 1253.6 eV used for the recrystallized $NaAlH_4$), which is more surface sensitive. We also observe a higher-energy doublet (red) in the spectra in Figure 3 that does not match the theoretical references, nor is it present in the lab-based experiments. The 2p features of period 3 elements have been shown to shift due to undercoordinated configurations,[46] such as for silicon, in which the 2p peaks for $HSiO_{3/2}$ can be shifted over 1 eV higher in binding energy than the stoichiometric oxide peak.[47] However, configurations including similar mixed hydride/oxide species such as $AlH_x(OH)_y$ have been simulated, and the binding energies for these species lie below that of Al_2O_3. Another possible explanation is local differential charging or another similar instrument effect, but other elements, including oxygen, do not exhibit comparable amounts of charging, even though shifts due to charging typically affect multiple peaks. Nonetheless, this high-energy doublet likely arises from an oxidic species given that, as the sample is heated, the shifting diminishes until the peaks merge with the unshifted Al−Ox features (blue). Species fractions derived from these fits are extracted from peak areas and shown in Figure 5 to illustrate the evolution of the surface chemistry during heating over time. Figure 5a shows the evolution of the amounts of shifted and unshifted Al−Ox and how, when they merge (after desorption), the total Al−Ox area is maintained.

As desorption starts, $NaAlH_4$ decomposes to produce additional Na_3AlH_6 and Al metal, the latter of which will spontaneously react with the neighboring O/OH species at the surface to be partially oxidized and become substoichiometric

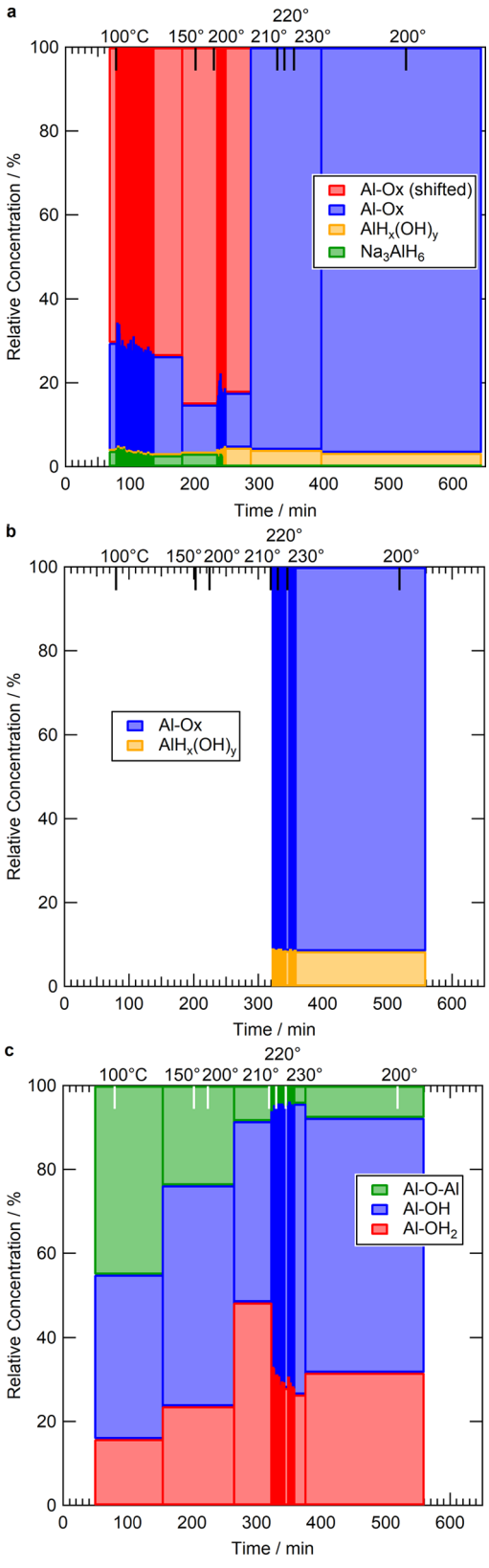

Figure 5. Relative amounts of each phase of (a, b) aluminum and (c) oxygen present at the surface obtained from detailed regional spectra at (a) PE = 440 eV and (b, c) PE = 735 eV.

oxides/hydroxides. As a result, we do not expect a significant surface signal from Al metal, as already discussed. However, an additional peak corresponding to these $AlH_x(OH)_y$ species does not appear until near maximum desorption (Figure 3b), which occurs at conditions commensurate with Na_3AlH_6 decomposition. At this stage, an additional intermediate region (orange curves, at ~73 eV) is found by fitting the Al 2p AP-XPS data, which is best assigned to the substoichiometric hydroxides based on the comparison with theory. With both experimental photon energies, each of these features was readily detectable. The greater PE of 735 eV sampled slightly deeper (~0.5 nm) into the surface and showed a greater proportion of more hydrogen-enriched aluminum (Figure S9), indicating that the hydrogen-poor aluminum species, including oxides and hydroxides, were primarily localized on the surface and not uniformly dispersed throughout the bulk.

From the Al 2p AP-XPS data alone, it is challenging to distinguish different surface oxide species. However, the O 1s spectra (Figure 4) give an unambiguous interpretation, with the deconvolution into three contributions closely matching both the theoretical predictions corresponding to the three distinct oxygen environments described above and previous experimental results for metal oxide, metal hydroxide, and strongly adsorbed hydroxide. Figure 4 presents the O 1s AP-XPS spectra collected for a sample before desorption, at maximum desorption, and in the final stages of desorption. Before desorption, the spectrum is dominated by the contributions from Al−O−Al and Al−OH, with only a small amount of surface $Al-OH_2$ species observed. Near the time of maximum desorption, the amount of Al−O−Al decreases from about 33% to about 5% of the oxygen content as the amounts and proportions of the species with higher hydrogen coordination increase, with the largest increase observed for $Al-OH_2$, which rises from only about 15% to near 50%. At elevated temperatures, after the majority of H_2 has already been desorbed, the $Al-OH_2$ signal decreases in favor of Al−OH. At the end of the in situ experiment, as well as in the ex situ desorbed sample, the oxygen was again mostly in the Al−OH form, with 25−30% as $Al-OH_2$ and 6−8% as Al−O. The three components shift by small amounts (~0.5 eV) throughout the experiment, indicating that subtle changes in the local configurations, in addition to the larger changes in the coordination of hydrogen, are taking place. However, these peak movements stay within the ranges predicted by the simulated theory configurations (indicated by the horizontal bars in Figure 4).

The data in Figure 4 indicate that the composition of the surface oxide evolves continuously during dehydrogenation, with initial hydrogen enrichment of the near-surface region followed by depletion. Presumably, the decrease of hydrogen content at the late stages of dehydrogenation is due to the decreased flux of H atoms from the bulk. No significant changes in O-containing gases in the mass spectra are seen over the course of the experiment, indicating that the extant oxygen remained on the sample and did not desorb as H_2O or O_2 from the reduction of the Al^{3+} species.

Surface Kinetic Mechanism. *Role of Titanium.* The absence of Ti at the surface (detectable at levels down to 0.1 atom %) invalidates many of the current mechanistic explanations for surface hydrogen evolution in the dehydrogenation of Ti-doped $NaAlH_4$, particularly those involving the formation of H_2 on metallic surface particles.[10] Several previous XPS studies of Ti-doped $NaAlH_4$ have observed the presence of surface titanium and attributed mechanistic roles to it; however, the detected concentration decreased substantially as the ball-milling time increased, and unin-

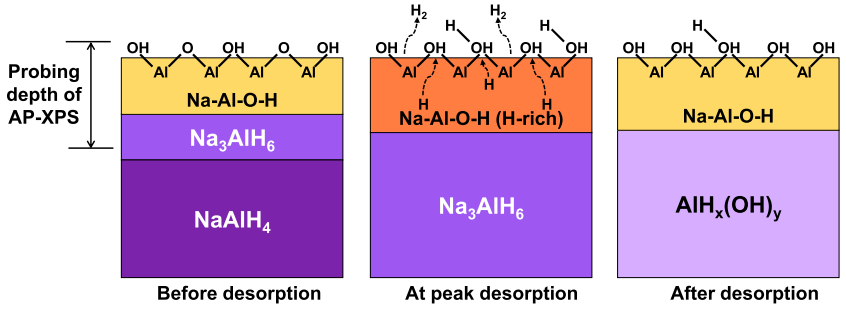

Figure 6. Schematic to illustrate the proposed evolution during dehydrogenation.

corporated $TiCl_3$ was detected in the briefly milled samples.[30,38] Léon et al. have shown that longer milling times improve the reaction kinetics,[48] indicating that the greater integration of Ti into the hydride and thus below the surface enhances the cycling rate. In our experiments, surface Ti is only detected when the sample has completed dehydrogenation. The demonstrated improvement in desorption kinetics must then be the result of Ti-promoted bulk or buried interface processes, such as defect formation, H diffusion, phase nucleation, and growth, or the "zipper model" of Na displacement from $NaAlH_4$ grains.[10] We cannot rule out the possibility that surface Ti could play a role in promoting rehydrogenation, which is not feasible at moderate pressures in pure sodium aluminum hydride,[9] though such investigation is beyond the scope of this study due to the subatmospheric pressure limitations of AP-XPS and LEIS.

Surface Oxygen Behavior. The existence and evolution of surface oxygen species over the course of hydrogen desorption, as shown in Figure 5c, reveal a richer mechanistic description of the surface kinetic processes. These oxidized moieties are unavoidable, as even the cleanest pure-Ar gloveboxes, where hydrides are synthesized and processed, contain traces of oxygen and water. It would take just a few seconds for those oxygenated species to interact with the highly reactive surface of $NaAlH_4$.[49,50] The good hydrogenation cyclability of our samples and crystallographic corroboration by XRD indicate that the bulk remains predominantly $NaAlH_4$, with some residual amounts of Na_3AlH_6 and no detected oxide or hydroxide, indicating that they are only thin surface structures, very highly disordered and noncrystalline, or present in very small quantities (Figure S6, Table S1). The predominant oxide species found at room temperature at the surface of the fully hydrogenated sample are metal oxide (Al−O−Al) and metal hydroxide (Al−OH). These different oxidized species likely result from the reaction of gaseous O_2 and/or H_2O with the AlH_4^- at the surface in different ratios, forming Na_3AlH_6 as a byproduct. Therefore, they are not expected to be present in an ordered, crystalline form, with the real experimental and AIMD-generated structures being substantially more complex.

Upon heating (70−100 °C), as mobile hydrogen within the Al−H clusters (AlH_4^- and AlH_6^{3-}) starts to migrate from the bulk toward the surface, most of the Al−O−Al becomes hydroxylated, Al−OH. $Al(OH)_3$ is known to conduct protons, even forming adsorbed species in the process,[51−53] and it has been found that Al_2O_3 can transmit H atoms over short distances on the surface without itself being reduced to the metal,[29] likely through transient formation of Al−OH species. At a slightly higher temperature (150 °C), a subtle but important transformation is observed, coinciding with a considerable increase in the release of hydrogen. This temperature likely corresponds to significant destabilization of bulk Na_3AlH_6, which is broadly consistent with previous reports of the Ti-doped Na−Al−H system.[25,54] More ionic Al−OH is destabilized by the H flux and evolves to more weakly bonded $Al-OH_2$ (distinct from physisorbed water), as clearly identified by AP-XPS shifts. The formation of these bound OH−H groups during dehydrogenation is key to our proposed mechanistic interpretation. As hydrogen atoms diffusing from the bulk reach the surface, the $Al-OH_2$ complex stabilizes the reaction intermediates for H_2 formation. The simplest way to explain the process is via the reaction of one protic H from an $Al-OH_2$ with a hydridic H coming from an Al−H species, generating H_2 and regenerating Al−OH. Although a possible pathway could have resulted in water formation (as typically occurs in hydroxylated oxide surfaces), we have not detected adsorbed water on the surface at a binding energy greater than that for the $Al-OH_2$ species.[55] Additionally, the total amount of oxygenated species on the surface remained mostly constant through the process, and neither gas-phase water nor oxygen was detected in the mass spectrum. The observed behavior can be explained with the following surface mechanism (eqs 3 and 4)

$$(Al-OH_2) + H \rightarrow (Al-OH) + H_2^{gas} \quad (3)$$

$$(Al-OH) + H \rightarrow (Al-OH_2) \quad (4)$$

Reactions 3 and 4 constitute a catalytic cycle, in which $Al-OH_2$ facilitates the kinetics, relative to a pristine surface with only Al−H moieties, but is not consumed in the process. Note that an analogous cycle between Al−O(−Al) and Al−OH can also be imagined. A complete description of the proposed phase evolution mechanism of $NaAlH_4$ surfaces during dehydrogenation is given in Figure 6.

In addition to providing some insight into the phase evolution of Ti-doped $NaAlH_4$ during dehydrogenation, the accumulation of hydrogen at the surface, as indicated by the hydroxylation of the oxide before and at peak desorption, reveals that a surface process is the rate-limiting step. We propose that the phase transition starts in the bulk, generating a supersaturation of hydrogen atoms in the material. At the initial stages of dehydrogenation, the surface still contains considerable amounts of oxide species, probably resulting in slow kinetics for hydrogen recombination and desorption. Slow surface desorption due to these oxides combined with relatively faster bulk dehydrogenation will result in an increased supersaturation of hydrogen at the subsurface. At certain supersaturation, surface oxides will not be in equilibrium with subsurface hydrogen and will hydroxylate, facilitating the kinetics for desorption and recombination (eqs 3 and 4). The supersaturation of subsurface hydrogen will

stabilize as the bulk and surface processes reach steady state. The surface hydroxylation will remain until the bulk fully dehydrogenates. The surface then returns to its initial mixture of oxides and hydroxides. Only operando measurements with highly sensitive surface spectroscopies could be capable of observing this hydroxylation process cycle.

It is unclear if the surface limitation arises from the slowing of the transport of H inside the oxidized aluminum layer compared to the hydride phases or from the already limited rate of the recombination reaction to form the gas. The activation energies for H transport in $NaAlH_4$, Na_3AlH_6,[56] and metallic Al[57] have been computed to be fairly similar, around 0.4 eV. However, the diffusion barrier in pure α-Al_2O_3 is 1.24 eV,[58] suggesting that transport may be hindered by the hydroxide layer, though the high degree of hydroxylation and number of defects may change the experimental value substantially.

Energetic Barriers. To understand better the potential impact of the oxide on the kinetics of H_2 formation, we modeled the surface dehydrogenation process in $NaAlH_4$ using nudged elastic band (NEB) calculations (see the Experimental Methods for details). To do so, we generated 10 different models based on characteristic AIMD-derived surfaces, from which the barriers for H_2 desorption were computed. Each model featured a pathway for H_2 desorption through which a H atom present in a surface OH^- group reacts with a nearby H in an AlH_4^- group and leaves the surface as a H_2 molecule. These pathways were compared to a similar pathway on the pristine surface without oxidation.

The results for the computed H_2 desorption barriers are shown in Figure 7. The barrier for H_2 extraction from idealized pristine $NaAlH_4$ was found to be 2.56 eV. On the other hand, the oxidized surfaces demonstrated far lower barriers ranging from 0.13 to 1.61 eV depending on the local surface features, with the lowest-barrier variants exhibiting a higher prevalence (Figure 7b; calculated mean = 0.68 eV). Reactions at the different oxidized surfaces followed very similar pathways, involving the reaction of a surface OH^- group with a H atom attached to an AlH_4^- group to form H_2 (Figure S10). In each case, the product incorporates the formation of a new bond between the O atom and the remaining AlH_3 group. In our simulations, this new binding configuration has a bond energy on the order of 0.5 eV or more, which helps stabilize the thermodynamics of H_2 release in addition to facilitating kinetics. Note that although the results shown in Figure 7 are for oxidized $NaAlH_4$, analogous behavior is expected for oxidized Na_3AlH_6. Previously reported barriers determined with DFT for a $NaAlH_4$ surface doped with an atom of Ti were about 1.5 eV,[59] which, though lower than that of the undoped surface, were more than twice the average barrier for the oxidized surfaces.

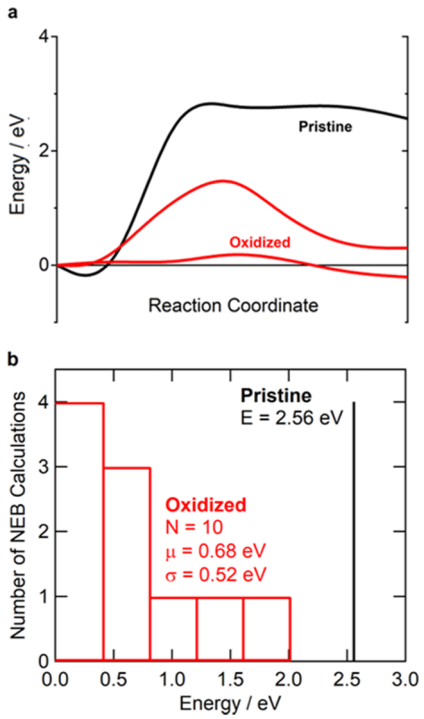

Figure 7. (a) Reaction coordinate diagram showing the evolution of energy over reaction paths for H_2 desorption from pristine (black) and two different oxidized $NaAlH_4$ surfaces (red) in NEB. (b) Histogram of barriers for H_2 desorption from all tested oxidized $NaAlH_4$ surfaces (red) compared with the value for the pristine surface (black).

The relatively low migration barriers calculated for the oxidized surfaces in Figure 7 likely arise from the charge states of the H atoms under investigation. In OH^- groups, H is present as a positively charged protonic species; in AlH_4^-, on the other hand, H atoms are present as negatively charged hydride ions. Thus, H_2 can be degassed from the material via a heterosynthetic process ($H^+ + H^- \rightarrow H_2$) that is much more kinetically favorable than the equivalent process in pristine $NaAlH_4$, whereby two hydride ions would need to part with two electrons in order to form H_2. This process also obviates the need for reduction of Al^{3+} at the surface. To validate the heterosynthetic nature of the H_2 formation pathway, we calculated the Bader charge profiles of the systems studied in our NEB calculations.[41,42] Indeed, H atoms in OH^- groups are positively charged within the Bader scheme (q = +0.99 ± 0.08), whereas H atoms in AlH_4^- groups are negatively charged (q = −1.00). This concept of heterosynthetic H_2 formation is not unique to this system; other complex hydrides, such as $(NH_4)^+(BH_4)^-$, are known to decompose readily in a similar manner.[60]

CONCLUSIONS

We have shown how observing the chemical evolution of surface species in dehydrogenating Ti-doped $NaAlH_4$ can elucidate which species may play an active role in dehydrogenation. The resulting operando evolution of surface and gas species was interpreted by DFT calculations and complemented by further ex situ characterization with several techniques to provide a precise microscopic picture of the Al and O surface species present. This approach allowed us to propose a mechanism to explain surface reactions in Ti-doped $NaAlH_4$ dehydrogenation: small amounts of Al−oxide impurities at the surface transform during desorption into Al−hydroxide species, which dynamically evolve according to hydrogen flux from the interior of the material. We propose that exchange among Al−O(−Al), Al−OH, and Al−OH_2 moieties at the surface may facilitate H_2 release within a catalytic cycle. This is reflected in NEB calculations, which show that dehydrogenation barriers are significantly lower on the oxidized surface as opposed to the pristine $NaAlH_4$ surface, which can be explained by the heterosynthetic reaction of negatively charged hydride ions bonded to Al and positively charged protonic species bonded to O.

As already indicated by previous studies, we confirmed that the surface of ball-milled $NaAlH_4$ is free of titanium, relegating its contribution in dehydrogenation to the bulk (where we have detected metallic Ti by STXM). This confirms that, in our analysis, Ti does not itself catalyze a surface process upon addition to pure $NaAlH_4$, as some studies have suggested. It is unclear from the above results what the role of titanium in the bulk is; numerous proposed mechanisms of action, including the improved nucleation and growth of product phases, the formation of AlH_x defects, and the facilitated transport of hydrogen within $NaAlH_4$, have been discussed in depth in the review by Frankcombe, though we cannot definitively affirm one of these with the surface science experiments we have conducted.[10] However, we find evidence of the accumulation of hydrogen in the near-surface region at intermediate stages of the reaction, indicating that the rate-determining process for the overall dehydrogenation of Ti-doped $NaAlH_4$ may switch to a surface process once Ti is added.

Our results strongly suggest that surface oxides are active participants in the surface dehydrogenation reaction. To support this hypothesis, we have provided a detailed view of the hydroxide-mediated chemistry in dehydrogenating $NaAlH_4$. Although the results presented here are limited to $NaAlH_4$, prevalent oxidation of the topmost surface layers can be expected in other complex metal hydrides, especially those that are extremely sensitive to residual oxidation such as the more gravimetrically capacious metal borohydrides. It is important to note that, in the absence of additional testing, the presence of a surface oxide cannot be directly linked to overall storage kinetics, given the possibility of other rate limitations not explored within our study. Nevertheless, we propose that controlling the dynamics of surface oxides and hydroxides, and how hydrogen diffuses and recombines at them, is a promising and largely unexplored route toward realizing the kinetic improvements needed for metal hydrides to meet vehicular-use targets.

■ ASSOCIATED CONTENT

Supporting Information

The Supporting Information is available free of charge on the ACS Publications website at DOI: 10.1021/acsami.8b17650.

Experimental methods for sample preparation, characterization, and theoretical calculations; hydrogen mass spectrum; additional XPS spectra; STXM images and XAS spectra; XRD pattern of cycled $NaAlH_4$; AIMD and NEB schematics; computed relative binding energies (PDF)

■ AUTHOR INFORMATION

Corresponding Authors

*E-mail: wood37@llnl.gov (B.C.W.).
*E-mail: felgaba@sandia.gov (F.E.G.).

ORCID

James L. White: 0000-0002-8216-7212
Lena Trotochaud: 0000-0002-8816-3781
Jinghua Guo: 0000-0002-8576-2172
Vitalie Stavila: 0000-0003-0981-0432
Hendrik Bluhm: 0000-0001-9381-3155
Mark D. Allendorf: 0000-0001-5645-8246
Brandon C. Wood: 0000-0002-1450-9719
Farid El Gabaly: 0000-0002-5822-9938

Author Contributions

The manuscript was written through contributions of all authors. All authors have given approval to the final version of the manuscript.

Notes

The authors declare no competing financial interest.

■ ACKNOWLEDGMENTS

This research used resources of the Advanced Light Source, which is a DOE Office of Science User Facility under contract no. DE-AC02-05CH11231 (Y.-S.L., L.T., J.G., H.B.). Part of the work was performed through a user project at the Molecular Foundry using its local computing cluster (Vulcan), which is managed by the High Performance Computing Service Group at the Lawrence Berkeley National Laboratory (L.F.W., D.P.) under Contract DE-AC02-05CH11231. Sandia National Laboratories (J.L.W., R.D.K., J.A.W., V.S., M.D.A, F.E.G.) is a multimission laboratory managed and operated by National Technology and Engineering Solutions of Sandia, LLC., a wholly owned subsidiary of Honeywell International, Inc., for the U.S. Department of Energy's National Nuclear Security Administration under contract DE-NA-0003525. This work was performed in part under the auspices of DOE by Lawrence Livermore National Laboratory under Contract DE-AC52-07NA27344 (A.J.E.R., L.F.W., S.K., T.O., A.A.B., J.R.I.L., B.C.W.). All authors gratefully acknowledge research support from the U.S. Department of Energy, Office of Energy Efficiency and Renewable Energy, Fuel Cell Technologies Office through the Hydrogen Storage Materials Advanced Research Consortium (HyMARC) and Sandia's Laboratory-Directed Research and Development Program. A.J.E.R. was supported by the National Science Foundation Graduate Research Fellowship Program under Grant No. 1650114. L.T. and H.B. acknowledge support by the Director, Office of Science, Office of Basic Energy Sciences, and by the Division of Chemical Sciences, Geosciences and Biosciences of the U.S. Department of Energy at LBNL under Contract No. DE-AC02-05CH11231. Dr. Norman Bartelt is thanked for fruitful discussions. Any opinions, findings, and conclusions or recommendations expressed in this material are those of the authors and do not necessarily reflect the views of the National Science Foundation, the U.S. Department of Energy, or the United States Government.

■ ABBREVIATIONS

AES, Auger electron spectroscopy
AIMD, ab initio molecular dynamics
AP-XPS, ambient-pressure X-ray photoelectron spectroscopy
DFT, density functional theory
DOE, U.S. Department of Energy
LEIS, low-energy ion scattering
PE, photon energy
STXM, scanning transmission X-ray microscopy
XAS, X-ray absorption spectroscopy
XPS, X-ray photoelectron spectroscopy
XRD, X-ray diffractometry

■ REFERENCES

(1) *Target Explanation Document: Onboard Hydrogen Storage for Light-Duty Fuel Cell Vehicles*; United States Department of Energy, 2017.

(2) Orimo, S.-i.; Nakamori, Y.; Eliseo, J. R.; Züttel, A.; Jensen, C. M. Complex Hydrides for Hydrogen Storage. *Chem. Rev.* **2007**, *107*, 4111−4132.
(3) Anton, D. L. Hydrogen Desorption Kinetics in Transition Metal Modified $NaAlH_4$. *J. Alloys Compd.* **2003**, *356*−*357*, 400−404.
(4) Streukens, G.; Bogdanović, B.; Felderhoff, M.; Schuth, F. Dependence of Dissociation Pressure upon Doping Level of Ti-doped Sodium Alanate-A Possibility for "Thermodynamic Tailoring" of the System. *Phys. Chem. Chem. Phys.* **2006**, *8*, 2889−2892.
(5) Bogdanović, B.; Eberle, U.; Felderhoff, M.; Schuth, F. Complex Aluminum Hydrides. *Scr. Mater.* **2007**, *56*, 813−816.
(6) Xuanhui, Q.; Ping, L.; Zhang, L.; Qi, W.; Iqbal, M. Z.; Rafique, M. Y.; Farooq, M. H. Superior Catalytic Effects of Nb_2O_5, TiO_2, and Cr_2O_3 Nanoparticles in Improving the Hydrogen Sorption Properties of $NaAlH_4$. *J. Phys. Chem. C* **2012**, *116*, 11924−11938.
(7) Pitt, M. P.; Vullum, P. E.; Sorby, M. H.; Emerich, H.; Paskevicius, M.; Buckley, C. E.; Gray, E. M.; Walmsley, J. C.; Holmestad, R.; Hauback, B. C. Amorphous $Al_{1-x}Ti_x$, $Al_{1-x}V_x$, and $Al_{1-x}Fe_x$ phases in the Hydrogen Cycled $TiCl_3$, VCl_3 and $FeCl_3$ enhanced $NaAlH_4$ systems. *J. Alloys Compd.* **2012**, *521*, 112−120.
(8) Li, L.; Xu, C.; Chen, C.; Wang, Y.; Jiao, L.; Yuan, H. Sodium Alanate System for Efficient Hydrogen Storage. *Int. J. Hydrogen Energy* **2013**, *38*, 8798−8812.
(9) Bogdanović, B.; Schwickardi, M. Ti-doped Alkali Metal Aluminium Hydrides as Potential Novel Reversible Hydrogen Storage Materials. *J. Alloys Compd.* **1997**, *253*−*254*, 1−9.
(10) Frankcombe, T. J. Proposed Mechanisms for the Catalytic Activity of Ti in $NaAlH_4$. *Chem. Rev.* **2012**, *112*, 2164−2178.
(11) Stavila, V.; Klebanoff, L.; Vajo, J.; Chen, P. Development of On-Board Reversible Complex Metal Hydrides for Hydrogen Storage. In *Hydrogen Storage Technology: Materials and Applications*; Klebanoff, L., Ed.; CRC Press: Boca Raton, 2013.
(12) Løvvik, O. M.; Opalka, S. A. Density Functional Calculations of Ti-Enhanced $NaAlH_4$. *Phys. Rev. B: Condens. Matter* **2005**, *71*, No. 054103.
(13) Li, S.; Ahuja, R.; Araujo, C. M.; Johansson, B.; Jena, P. Dehydrogenation Associated with Ti Catalyst in Sodium Alanate. *J. Phys. Chem. Solids* **2010**, *71*, 1073−1076.
(14) Dathara, G. K. P.; Mainardi, D. S. Structure and Dynamics of Ti-Al-H Compounds in Ti-doped $NaAlH_4$. *Mol. Simul.* **2008**, *34*, 201−210.
(15) Brinks, H. W.; Hauback, B. C.; Srinivasan, S. S.; Jensen, C. M. Synchrotron X-ray Studies of $Al_{1-y}Ti_y$ Formation and Re-hydriding Inhibition in Ti-Enhanced $NaAlH_4$. *J. Phys. Chem. B* **2005**, *109*, 15780−15785.
(16) Pitt, M. P.; Vullum, P. E.; Sørby, M. H.; Blanchard, D.; Sulic, M. P.; Emerich, H.; Paskevicius, M.; Buckley, C. E.; Walmsley, J.; Holmestad, R.; Hauback, B. C. The Location of Ti Containing Phases after the Completion of the $NaAlH_4$ + x$TiCl_3$ Milling Process. *J. Alloys Compd.* **2012**, *513*, 597−605.
(17) Pitt, M. P.; Vullum, P. E.; Sørby, M. H.; Emerich, H.; Paskevicius, M.; Buckley, C. E.; Gray, E. M.; Walmsley, J. C.; Holmestad, R.; Hauback, B. C. Crystalline $Al_{1-x}Ti_x$ Phases in the Hydrogen Cycled $NaAlH_4$ + 0.02$TiCl_3$ System. *Philos. Mag.* **2013**, *93*, 1080−1094.
(18) Chaudhuri, S.; Graetz, J.; Ignatov, A.; Reilly, J. J.; Muckerman, J. T. Understanding the Role of Ti in Reversible Hydrogen Storage as Sodium Alanate: A Combined Experimental and Density Functional Theoretical Approach. *J. Am. Chem. Soc.* **2006**, *128*, 11404−11415.
(19) Wang, J.; Ebner, A. D.; Prozorov, T.; Zidan, R.; Ritter, J. A. Effect of Graphite as a Co-dopant on the Dehydrogenation and Hydrogenation Kinetics of Ti-doped Sodium Aluminum Hydride. *J. Alloys Compd.* **2005**, *395*, 252−262.
(20) Léon, A.; Kircher, O.; Rothe, J.; Fichtner, M. Chemical State and Local Structure Around Titanium Atoms in $NaAlH_4$ doped with $TiCl_3$ Using X-ray Absorption Spectroscopy. *J. Phys. Chem. B* **2004**, *108*, 16372−16376.
(21) Haiduc, A. G.; Stil, H. A.; Schwarz, M. A.; Paulus, P.; Geerlings, J. J. C. On the Fate of the Ti Catalyst During Hydrogen Cycling of Sodium Alanate. *J. Alloys Compd.* **2005**, *393*, 252−263.
(22) Léon, A.; Finck, N.; Rothe, J.; Felderhoff, M.; Fichtner, M. Fluorescence X-ray Absorption Study of $ScCl_3$-Doped Sodium Alanate. *J. Phys. Chem. C* **2015**, *119*, 15810−15815.
(23) Léon, A.; Balerna, A.; Cinque, G.; Frommen, C.; Fichtner, M. Al K edge XANES Measurements in $NaAlH_4$ doped with $TiCl_3$ by Ball Milling. *J. Phys. Chem. C* **2007**, *111*, 3795−3798.
(24) Graetz, J.; Reilly, J. J.; Johnson, J.; Ignatov, A. Y.; Tyson, T. A. X-ray Absorption Study of Ti-Activated Sodium Aluminum Hydride. *Appl. Phys. Lett.* **2004**, *85*, 500−502.
(25) Gross, K. J.; Sandrock, G.; Thomas, G. J. Dynamic In Situ X-ray Diffraction of Catalyzed Alanates. *J. Alloys Compd.* **2002**, *330*−*332*, 691−695.
(26) Ivancic, T. M.; Hwang, S.-J.; Bowman, R. C.; Birkmire, D. S.; Jensen, C. M.; Udovic, T. J.; Conradi, M. S. Discovery of a New Al Species in Hydrogen Reactions of $NaAlH_4$. *J. Phys. Chem. Lett.* **2010**, *1*, 2412−2416.
(27) Sorte, E. G.; Bowman, R. C.; Majzoub, E. H.; Verkuijlen, M. H. W.; Udovic, T. J.; Conradi, M. S. Mobile Species in $NaAlH_4$. *J. Phys. Chem. C* **2013**, *117*, 8105−8113.
(28) Jeon, K.-J.; Moon, H. R.; Ruminski, A. M.; Jiang, B.; Kisielowski, C.; Bardhan, R.; Urban, J. J. Air-Stable Magnesium Nanocomposites Provide Rapid and High-Capacity Hydrogen Storage Without Using Heavy-Metal Catalysts. *Nat. Mater.* **2011**, *10*, 286−290.
(29) Karim, W.; Spreafico, C.; Kleibert, A.; Gobrecht, J.; VandeVondele, J.; Ekinci, Y.; van Bokhoven, J. A. Catalyst Support Effects on Hydrogen Spillover. *Nature* **2017**, *541*, 68−71.
(30) Delmelle, R.; Gehrig, J. C.; Borgschulte, A.; Züttel, A. Reactivity Enhancement of Oxide Skins in Reversible Ti-doped $NaAlH_4$. *AIP Adv.* **2014**, *4*, No. 127130.
(31) Yeh, J. J.; Lindau, I. Atomic Subshell Photoionization Cross Sections and Asymmetry Parameters: $1 \leqslant Z \leqslant 103$. *At. Data Nucl. Data Tables* **1985**, *32*, 1−155.
(32) Moulder, J. F.; Stickle, W. F.; Sobol, P. E.; Bomben, K. D. *Handbook of X-ray Photoelectron Spectroscopy*; Perkin-Elmer Corporation: Eden Prairie, MN, 1992.
(33) McGuire, G. E.; Schweitzer, G. K.; Carlson, T. A. Core Electron Binding Energies in Some Group IIIA, VB, and VIB Compounds. *Inorg. Chem.* **1973**, *12*, 2450−2453.
(34) Do, T.; McIntyre, N. S.; Harshman, R. A.; Lundy, M. E.; Splinter, S. J. Application of Parallel Factor Analysis and X-ray Photoelectron Spectroscopy to the Initial Stages in Oxidation of Aluminium. I. The Al 2p Photoelectron Line. *Surf. Interface Anal.* **1999**, *27*, 618−628.
(35) Arata, K.; Hino, M. Solid Catalyst Treated with Anion: XVIII. Benzoylation of Toluene with Benzoyl Chloride and Benzoic Anhydride Catalysed by Solid Superacid of Sulfate-Supported Alumina. *Appl. Catal.* **1990**, *59*, 197−204.
(36) Lindsay, J. R.; Rose, H. J.; Swartz, W. E.; Watts, P. H.; Rayburn, K. A. X-ray Photoelectron Spectra of Aluminum Oxides: Structural Effects on the "Chemical Shift". *Appl. Spectrosc.* **1973**, *27*, 1−5.
(37) Crist, B. V. *Handbooks of Monochromatic XPS Spectra*; XPS International, Inc.: Ames, IA, 1999.
(38) Léon, A.; Schild, D.; Fichtner, M. Chemical State of Ti in Sodium Alanate Doped with $TiCl_3$ Using X-ray Photoelectron Spectroscopy. *J. Alloys Compd.* **2005**, *404*−*406*, 766−770.
(39) Paul, J.; Hoffmann, F. M. Decomposition of Water on Clean and Oxidized Aluminum(100). *J. Phys. Chem.* **1986**, *90*, 5321−5324.
(40) Pham, T. A.; Zhang, X.; Wood, B. C.; Prendergast, D.; Ptasinska, S.; Ogitsu, T. Integrating Ab Initio Simulations and X-ray Photoelectron Spectroscopy: Toward A Realistic Description of Oxidized Solid/Liquid Interfaces. *J. Phys. Chem. Lett.* **2018**, *9*, 194−203.
(41) Henkelman, G.; Arnaldsson, A.; Jónsson, H. A Fast and Robust Algorithm for Bader Decomposition of Charge Density. *Comput. Mater. Sci.* **2006**, *36*, 354−360.

(42) Tang, W.; Sanville, E.; Henkelman, G. A Grid-Based Bader Analysis Algorithm Without Lattice Bias. *J. Phys.: Condens. Matter* **2009**, *21*, No. 084204.
(43) Kang, X. D.; Wang, P.; Cheng, H. M. Improving Hydrogen Storage Performance of $NaAlH_4$ by Novel Two-Step Milling Method. *J. Phys. Chem. C* **2007**, *111*, 4879−4884.
(44) Wan, C. B.; Ju, X.; Qi, Y.; Wang, S. M.; Liu, X. P.; Jiang, L. J. Synchrotron X-ray Diffraction and X-ray Photoelectron Spectroscopy Studies of $NaAlH_4$ Containing Ti-Zr Hydride Additives. *J. Alloys Compd.* **2009**, *486*, 436−441.
(45) Aeschlimann, J. *The Dynamics of Sodium Alanate Based Hydrogen Storage Materials and Their Associated X-ray Absorption Spectroscopy*; ETH Zürich: Zürich, Switzerland, 2016.
(46) Kirsch, P. D.; Kang, C. S.; Lozano, J.; Lee, J. C.; Ekerdt, J. G. Electrical and Spectroscopic Comparison of HfO_2/Si Interfaces on Nitrided and Un-nitrided Si(100). *J. Appl. Phys.* **2002**, *91*, 4353−4363.
(47) Nordberg, R.; Brecht, H.; Albridge, R. G.; Fahlman, A.; Van Wazer, J. R. Binding Energy of the "2p" Electrons of Silicon in Various Compounds. *Inorg. Chem.* **1970**, *9*, 2469−2474.
(48) Léon, A.; Kircher, O.; Fichtner, M.; Rothe, J.; Schild, D. Evolution of the Local Structure Around Ti Atoms in $NaAlH_4$ Doped with $TiCl_3$ or Ti_{13}•6THF by Ball Milling Using X-ray Absorption and X-ray Photoelectron Spectroscopy. *J. Phys. Chem. B* **2006**, *110*, 1192−1200.
(49) Dai, B.; Rankin, R. B.; Johnson, J. K.; Allendorf, M. D.; Sholl, D. S.; Zarkevich, N. A.; Johnson, D. D. Influence of Surface Reactions on Complex Hydride Reversibility. *J. Phys. Chem. C* **2008**, *112*, 18270−18279.
(50) Schülke, M.; Paulus, H.; Lammers, M.; Kiss, G.; Réti, F.; Müller, K.-H. Influence of Surface Contaminations on the Hydrogen Storage Behaviour of Metal Hydride Alloys. *Anal. Bioanal. Chem.* **2008**, *390*, 1495−1505.
(51) Freund, F.; Wengeler, H. Proton Conductivity of Simple Ionic Hydroxides Part I: The Proton Conductivities of $Al(OH)_3$, $Ca(OH)_2$, and $Mg(OH)_2$. *Ber. Bunsen-Ges. Phys. Chem.* **1980**, *84*, 866−873.
(52) Wengeler, H.; Martens, R.; Freund, F. Proton Conductivity of Simple Ionic Hydroxides Part II: In Situ Formation of Water Molecules Prior to Dehydration. *Ber. Bunsen-Ges. Phys. Chem.* **1980**, *84*, 873−880.
(53) Teng, H.-T.; Lee, T.-Y.; Chen, Y.-K.; Wang, H.-W.; Cao, G. Effect of $Al(OH)_3$ on the Hydrogen Generation of Aluminum−Water System. *J. Power Sources* **2012**, *219*, 16−21.
(54) Kiyobayashi, T.; Srinivasan, S. S.; Sun, D.; Jensen, C. M. Kinetic Study and Determination of the Enthalpies of Activation of the Dehydrogenation of Titanium- and Zirconium-Doped $NaAlH_4$ and Na_3AlH_6. *J. Phys. Chem. A* **2003**, *107*, 7671−7674.
(55) El Gabaly, F.; McDaniel, A. H.; Grass, M.; Chueh, W. C.; Bluhm, H.; Liu, Z.; McCarty, K. F. Electrochemical Intermediate Species and Reaction Pathway in H_2 Oxidation on Solid Electrolytes. *Chem. Commun.* **2012**, *48*, 8338−8340.
(56) Shi, Q.; Voss, J.; Jacobsen, H. S.; Lefmann, K.; Zamponi, M.; Vegge, T. Point Defect Dynamics in Sodium Aluminum Hydrides - A Combined Quasielastic Neutron Scattering and Density Functional Theory Study. *J. Alloys Compd.* **2007**, *446−447*, 469−473.
(57) Zhou, X. W.; El Gabaly, F.; Stavila, V.; Allendorf, M. D. Molecular Dynamics Simulations of Hydrogen Diffusion in Aluminum. *J. Phys. Chem. C* **2016**, *120*, 7500−7509.
(58) Belonoshko, A. B.; Rosengren, A.; Dong, Q.; Hultquist, G.; Leygraf, C. First-Principles Study of Hydrogen Diffusion in Al_2O_3 and Liquid Alumina. *Phys. Rev. B* **2004**, *69*, No. 024302.
(59) Ljubić, I.; Clary, D. C. Towards Understanding a Mechanism for Reversible Hydrogen Storage: Theoretical Study of Transition Metal Catalysed Dehydrogenation of Sodium Alanate. *Phys. Chem. Chem. Phys.* **2010**, *12*, 4012−4023.
(60) Karkamkar, A.; Kathmann, S. M.; Schenter, G. K.; Heldebrant, D. J.; Hess, N.; Gutowski, M.; Autrey, T. Thermodynamic and Structural Investigations of Ammonium Borohydride, a Solid with a Highest Content of Thermodynamically and Kinetically Accessible Hydrogen. *Chem. Mater.* **2009**, *21*, 4356−4358.